JOURNAL OF CHEMICAL PHYSICS VOLUME 120, NUMBER 16 22 APRIL 2004

Dynamics and the breaking of a driven cage: I_2 in solid Ar

Z. Bihary, R. Zadoyan, M. Karavitis, and V. A. Apkarian[a]
Department of Chemistry, University of California, Irvine, California 92697

(Received 29 August 2003; accepted 4 February 2004)

Pump–probe measurements of I_2 in solid Ar are reported and analyzed to extract a description of cage response to impulsive excitation, from the gentle kick, up to the breaking point. The most informative data are obtained through wavepacket motion on cage-bound, but otherwise dissociative, potentials where the chromophore acts as a transducer to drive the cage and to report on the local dynamics. This general class of dynamics is identified and analyzed as a function of energy in Ar, Kr, and Xe. The overdriven cage rebounds with a characteristic period of 1.2 ps that shows little dependence on excitation amplitude, in all hosts. After rebound, the cage rings as a local resonant mode in Ar, with a period of 1 ps and dephasing time of 3 ps. This mode remains at the Debye edge in Kr and Xe, with periods of 630 and 800 fs, and dephasing times of 8 and 6 ps, respectively. In the bound *B*-state, the cage fluctuates toward its dilated equilibrium structure on a time scale of 3 ps, which is extracted from the down-chirp in the molecular vibrational frequency. When kicked with excess energy of 4 eV, the Ar cage breaks with 50% probability, and the molecule dissociates. The kinetics of polarization selective, multiphoton dissociation with Gaussian laser intensity profiles is delineated and the ballistics of cage breakout is described: The photodissociation proceeds by destruction of the local lattice, by creating interstitials and vacancies. During large amplitude motion on cage-bound potentials, sudden, nonadiabatic spin–flip transitions can be observed and quantified in space and time. The spin–flip occurs with unit probability in Ar when the I^*-I bond is stretched beyond 6 Å. © *2004 American Institute of Physics.*
[DOI: 10.1063/1.1689958]

I. INTRODUCTION

Pump–probe studies of iodine isolated in matrix Ar were reported from our laboratory as the first example of ultrafast time-resolved investigations in matrices.[1,2] Subsequently, the more extensive studies were carried out in matrices of Kr,[3–6] and to a lesser extent in Xe,[7] in part due to signal degradation by permanent photo-dissociation of the molecule in Ar. The phenomenon is of interest since it involves the breaking of the prototypical cage. In contrast with prior case studies of photodissociation in matrices,[8] the large mass asymmetry in this case leads to a qualitatively different mechanism of cage breakout, as we highlight. We succinctly reported on this process in a recent four-wave mixing study in I_2-Ar, since it was essential to take it into account in the data reduction.[9] The dissociation occurs photo-selectively, through multiphoton excitation, at a rate slow enough to allow time-resolved studies on the intact molecule. We use the molecule in its various electronic states to characterize dynamics of the relatively soft cage when driven up to, and including, the breaking point. Through pump–probe measurements and classical molecular-dynamics simulations we analyze three characteristic behaviors:

(a) Cage response to dynamics on the bound B-state;
(b) cage dynamics when the molecule is prepared on a dissociative surface which is strictly bound by the cage (cage-bound potential);
(c) breaking of the cage.

The common theme in these analyses is the use of a molecular spring of variable stiffness to drive and sense the cage response—an analogy already made in the interpretation of emission spectra from cage-bound potentials.[10] Cage motion, as distinct from the chromophore vibration, can be observed in pump–probe data.[1,2,6] On the deeply bound *B*-state of I_2,[4–6,11–13] the intermolecular vibration dominates. In contrast, on dissociative molecular potentials, the dominant dynamics is that of the cage. This, we show through experiments and simulations in Ar, and extend it to the parallel dynamics in Kr and Xe. The analysis forces revision of our prior interpretation of persistent cage oscillations observed in Kr, which were attributed to a dynamical resonance between chromophore and cage.[6] Indeed, the same oscillations in Kr have been reproduced and extended by Schwentner *et al.*, using a variety of preparation schemes.[14] They recognize the generic nature of the oscillations, but ascribe them to zone-boundary phonons. Closely related to the present investigation are studies of cage dynamics in Ar, in which Rydberg transitions of NO were used to sense cage motion.[15–17] With the theoretical analyses of impulsive excitation in our prototypical system as background,[18–20] a detailed picture of mechanical accommodation is sought.

Beyond atomistic mechanics, the fate of the internal electronic degrees of freedom of the chromophore is of intimate relevance. In this regard, due to the legacy of investigations in the liquid phase,[21–23] and in clusters,[24,25] the predissociation of the *B*-state of I_2 has been pursued in matrices,

---

[a] Electronic mail address: aapkaria@uci.edu

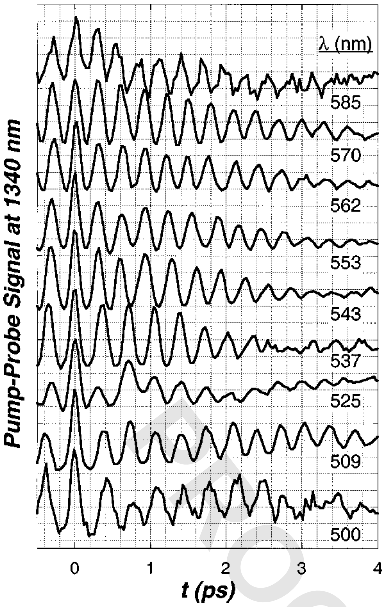

FIG. 1. Single color pump–probe measurements in $I_2-Ar(s)$, while monitoring NIR fluorescence at 1340 nm. The signal probes wavepacket motion on the *B*-state of iodine.

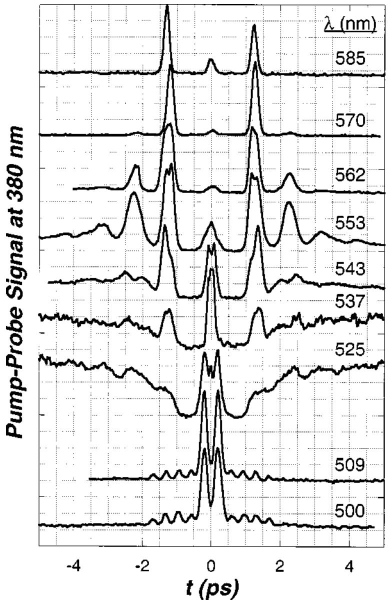

FIG. 2. Single color pump–probe measurements in $I_2-Ar(s)$, while monitoring UV fluorescence at 380 nm. At wavelengths between 585 and 525 nm, strictly motion on cage-bound potentials is observed, while at 509 and 500 nm, the modulation after the first resonance is from the *B*-state.

both experimentally,[4,13,26] and theoretically.[27,28] These studies underscore the important role played by details of cage dynamics in determining nonadiabatic transitions. Given the dense manifold of electronic states in I_2, nonadiabatic transitions can occur on a multitude of surfaces, as illustrated in the simulations using the full electronic manifold.[27,28] Large amplitude vibrations on cage-bound potentials provide a unique window for the precise determination of collision induced spin–flip transitions, such as have been recently demonstrated in real-time in the closely related ClF–Ar system.[29,30]

II. EXPERIMENT

The experimental methods used in our pump–probe studies of matrix isolated iodine have been extensively reported previously. Briefly, we deposit a thin film of the premixed gaseous sample, at a mixing ratio of 1:5000, on a cold window. The sample is then interrogated with near transform limited ~70 fs pulses derived from optical parametric amplifiers driven by a Kerr lens mode locked and regeneratively amplified Ti:Sapphire laser. The signal consists of laser induced fluorescence recorded as a function of delay between pump and probe pulses that are focused on the sample. In the main set of experimental data to be reported, we simultaneously monitor NIR and ultraviolet (UV) fluorescence. A liquid nitrogen cooled Ge detector is used for the former, while a photomultiplier is used for the latter, each placed behind a separate monochromator.

III. RESULTS

Single color pump–probe measurements were carried out at $\lambda = 585-500$ nm while simultaneously monitoring NIR and UV fluorescence at 1340 and 380 nm, respectively. The data are shown in Figs. 1 and 2. The NIR emission shows the characteristic *B*-state recursions, with a period of ~300 fs, riding over a slowly evolving background. The UV detected signal is dramatically different. At $\lambda = 525-585$ nm, the first recursion in the signal occurs at 1.2 ps, followed by strongly damped oscillations. This signal will be assigned to motion on cage-bound potentials. At $\lambda = 509$ and 500 nm, after a single intense recursion, the *B*-state contribution with its characteristic period of 300 fs is seen (Fig. 2). The UV spectra responsible for the observed dynamics are inspected through two-color measurements, 550 nm/595 nm. A two-dimensional plot of spectrum versus time delay is shown in Fig. 3(a), along with time slices at 380 and 305 nm. Spectral slices are shown in Fig. 3(b). When pumped with 550 nm and probed at 595 nm, the *B*-state signal is observed identically in the pair of intense bands at 395 and 305 nm, with a weaker contribution at 331 nm. When pumped at 595 nm and probed at 550 nm, the emission at 380 nm shows the cage-bound motion observed in the single color measurements of Fig. 2.

In Ar, all observed signals permanently decay with time due to multi-photon induced dissociation which proceeds without scrambling of molecular orientation.[9] The experimental geometry used to demonstrate this is shown in the inset to Fig. 4. Two cross-polarized beams of equal intensity, at $\lambda = 550$ nm, are brought into focus on the sample with a small angle of incidence. The overlap of beams within the focal volume is ensured by optimizing the coherent anti-Stokes Raman Spectroscopy (CARS) signal from iodine.[9] The UV fluorescence is monitored as a function of irradiation time with one beam on. After the signal decays to ~10% of its initial value, the beams are switched, and LIF from the same volume is monitored. The signal decay is nonexponential. Upon switching beams, the intensity jumps, indicating the polarization selectivity of the decay. The decay profile in

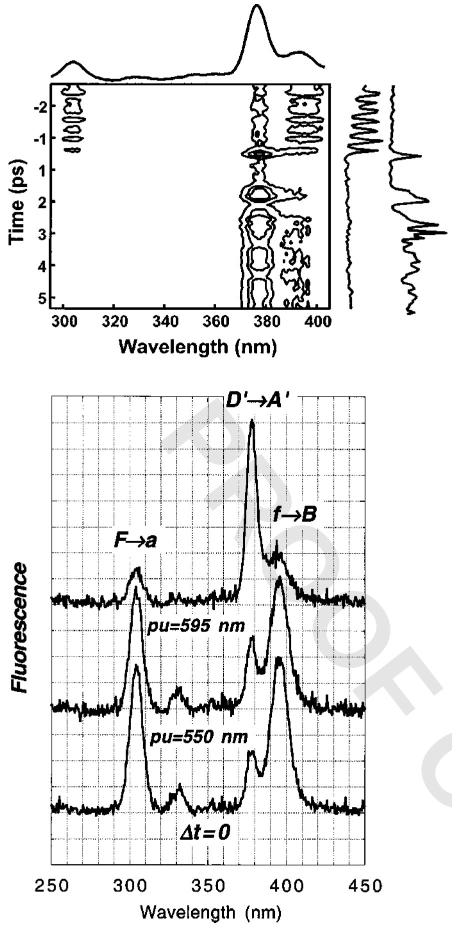

FIG. 3. (a) Contour plot of two-color pump–probe measurements, 550 nm/595 nm, while recording the UV spectrum. The spectral slice is obtained at zero delay between pump and probe pulses. The time slices illustrate that when pumped with 550 nm and probed with 595 nm, the emissions at 305 and 395 nm show the *B*-state motion; when pump and probe roles are reversed, the emission at 380 nm shows the cage-bound motion. (b) The assigned UV emission bands from the ion-pair states, obtained in 550 nm/595 nm pump–probe measurements. Lower trace obtained at zero delay. In the middle trace, 550 nm pulse acts as pump. The $D'(2g)$ state belongs to the first tier of ion pair states, while the $f(0_g)$ and $F(0_u)$ state belong to the second tier.

the second cycle is distinct from the first, and the dramatic slow-down leads to a plateau that persists. The sample degradation limits the achievable signal-to-noise ratio in measurements. In the single color measurements, we take advantage of time-symmetry to correct for the decaying baseline.[9]

IV. DISCUSSION

Molecular iodine has a dense manifold of electronic states in the UV-VIS spectral range,[31] providing rich opportunities for staging and investigating photophysics. Characterization of the solvated potentials is an integral part of time-resolved studies, and a great deal of such information has emerged from time and frequency domain studies in matrices.[32–35] A good guide for assignments is provided through the sudden. (''Sudden'' implies molecular potentials evaluated in a lattice frozen at its equilibrium geometry on the ground state.) Diatomics in molecule (DIM) potentials of Batista and Coker,[28,36] which are shown in Fig. 5. The manifold contains the covalent states, with asymptotic limits I $+$I, I$^*+$I, I$^*+$I*, separated by the spin–orbit splitting of $\Delta\sim 1$ eV; and the three tiers of ion-pair states,[37] I^+I^-, with a spread of 1 eV, starting 1 eV above the I*I* limit [throughout, $I^*\equiv I(^2P_{1/2})$ and $I\equiv I(^2P_{3/2})$.] The potentials of principle relevance are highlighted in Fig. 5(a). Their identification is discussed in each section below. Effective potentials, which are designed to simulate dynamics on the dissociative cage-bound I*–I*, I*–I, and I–I potentials, are shown in Fig. 5(b).

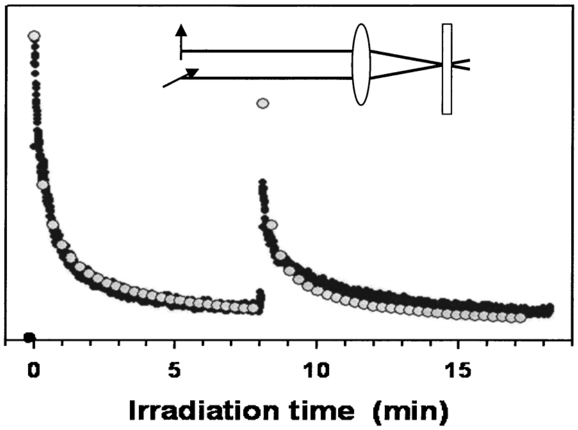

FIG. 4. Permanent depletion of fluorescence, at $\lambda=380$ nm, as a function of irradiation time, at $\lambda=550$ nm. The experimental arrangement consists of two cross-polarized beams that focus on the same spot. The sample is first irradiated with one beam, then the other. The white circles represent the fit to both cycles, taking into account both angular anisotropy and intensity distribution of the beams in the focal volume (see Appendix).

A. Dynamics on the bound *B*-state

1. Spectroscopic considerations

The characteristic period of oscillations in the pump–probe measurements using the NIR emission (Fig. 1) establishes that the observed evolution is that of a packet on the *B*-state. The observation of a peak at $t=0$, establishes that the pump and probe windows are vertically above each other in the range of measurements: $\lambda=500$–585 nm, (34 000–40 000 cm^{-1}). The monitored emission at 1340 nm has been assigned previously to the $I^*I^*(0_u^-)\rightarrow I^*I(0_g^-)$ spin-flip transition.[38] Based on $u\leftrightarrow g$ selection rules, the emitting state cannot be directly accessed optically. Based on Mulliken's sorting of the repulsive potentials in this range,[31] and dipole selection rules, the probe transition can be fairly uniquely assigned to: $I^*I^*[{}^1\Sigma_g^+(0^+)]\leftarrow I^*I[B({}^3\Pi_{0u})]$, with subsequent population transfer to $I^*I^*(O_u^-)$ and fluorescence. This suggests an upward correction of the $I^*I^*[{}^1\Sigma_g^+(0^+)]$ potential at the ground-state minimum by as much as 5000 cm^{-1}, as already suggested in the re-analysis of emission from this state.[10]

The *B*-state packet is also observed in the two-dimensional (2D) spectrum of Fig. 3, through the 305 and 395 nm ion-pair emissions induced by pumping at 550 nm and probing at 595 nm. Based on energy conservation alone, emission at 305 nm implies that the *B*-state is being probed by two-photon excitation at 595 nm. Based on the observa-

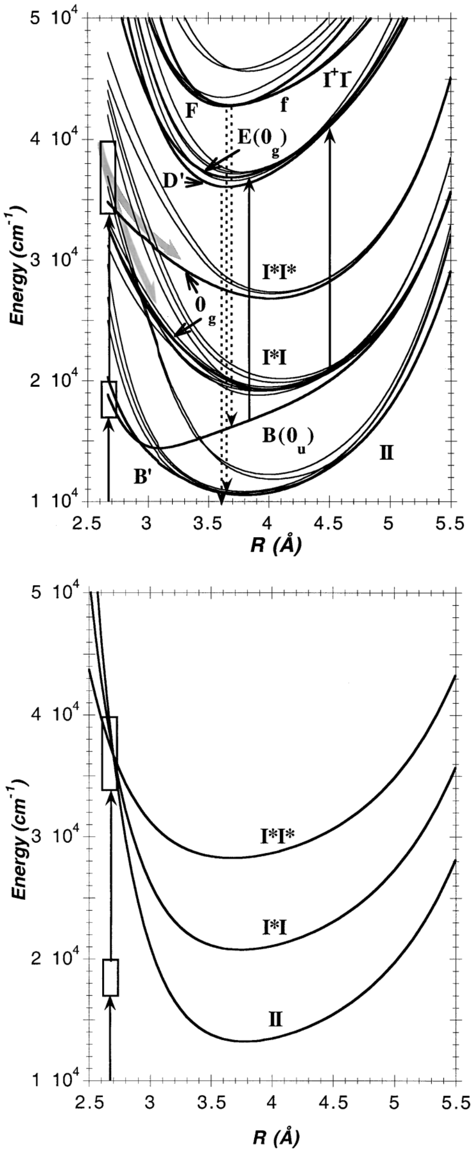

FIG. 5. (a) Sudden electronic potentials of iodine in solid Ar. The boxes indicate the one-photon and two-photon accessible range in the experiments, for $\lambda = 585-500$ nm. The *B*-state is probed via vertical $1+1$ excitation, while monitoring fluorescence over the I*I*→I*I spin-flip transition at 1340 nm (Fig. 1). The vertical up-arrows correspond to probing at 500 nm, which allows the simultaneous interrogation of both the *B*-state and I*I states via the first tier ion-pair states, by monitoring fluorescence over $D' \rightarrow A'$ (Fig. 2). The dashed arrows correspond to the emissions observed in Fig. 3(b). (b) The sudden potentials used in the simulations. These are constructed as Morse potentials along the I–I coordinate, fit to reproduce vertical excitation at the ground state minimum, and made to approximate the minima in sudden potentials of (b). The parameters are given in the text.

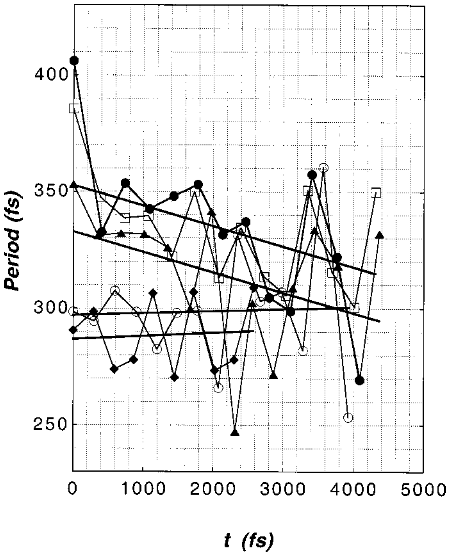

FIG. 6. The periods of motion of $I_2(B)$ in Ar, for initial preparation energies determined by the pump wavelengths: (●) 500 nm, (□) 509 nm, (▲) 537 nm, (○) 570 nm, (◆) 585 nm. Best fit lines are included to show the trend of fluctuations as the system equilibrates.

tion of signal at zero-delay, the pump and probe windows must be vertically aligned. Energetically, the vertical $1+2$ excitation of $52\,000$ cm^{-1} reaches the second tier of ion-pair states, and the observed emissions can be consistently assigned to originate from there. The 395 nm band can be recognized as the $f(0_g) \rightarrow B(0_u)$ transition, previously used to probe the *B*-state.[4] The 305 nm emission must terminate on the $I+I$ asymptote; and its intensity, which is comparable to the 395 nm band, suggests that it is a $\Delta\Omega = 0$ transition from the second tier, identifying it as $F(0_u) \rightarrow a(0_g)$. Recently, the 395 nm band was assigned to $D' \rightarrow A'$, but from a "secondary" site.[34] This cannot be according to the 2D plot of Fig. 3(a), which shows the 380 and 395 nm bands to have completely different time dependence. We see no evidence for site multiplicity. The main basis of this assignment in Ref. 34 seems to be the observation of differential bleaching. Rather than site-selective bleaching, we suggest below that this arises from polarization selective photodissociation. The information content of the data in Fig. 3 is complimentary to the NIR fluorescence, which is the set to be used for the analysis of *B*-state dynamics. The data also illustrates the ubiquity of multi-photon processes in the system, which will be a recurring theme below.

2. Accommodation by the tight cage

Molecular iodine fits tightly in the double substitutional site of solid Ar. That this is the isolation site, has been established with some confidence in the recent vibrational analysis of the ground state using time resolved four-wave mixing experiments[39] and vibrational self-consistent field theory.[40] Upon promotion to the *B*-state, the molecule undergoes large amplitude vibrations, relaxing toward the *B*-state minimum where the bond is ~0.3 Å longer than in the ground state. The cage must expand to accommodate the elongated molecule, and the suddenly driven cage can be expected to oscillate toward its final equilibrium configuration. The molecular vibrational frequency in the *B*-state, 128 cm^{-1} in the gas phase,[41] is nearly twice the Debye limit of solid Ar of 65 cm^{-1}.[42] Thus, we may expect chatter between cage and molecule, as the system solvates. This is observable as fluctuations in the periods of motion as a function of time, as shown in Fig. 6. Let us highlight the information content in this figure.

At the highest energy prepared, at 500 nm, the motion starts with a period of 410 fs, and dramatically drops below 350 fs by the second period. The periods then oscillate

COPY 020416JCP

around a declining mean, reaching 300 fs after 15 cycles. This preparation energy is near the gas phase dissociation limit of the *B*-state. As such, the attractive wall of the potential in this region is dominated by the cage. This highly anharmonic region leads to strongly nonlinear dynamics and dramatic energy loss upon first collision, followed by a milder and linear rate of vibrational energy flow—a generic behavior, previously highlighted in studies of the *A*-state in Ar and Kr,[2] and the *B*-state in Kr.[4] The contraction of periods reflects vibrational relaxation. If a static solvated potential is assumed, then the period can be related to energy. Such an analysis has been gainfully implemented in Kr to extract energy flow rates directly from experiments.[11–13] However, the reduction in terms of a mean potential misses dynamics of the cage and time-dependence of accommodation (solvation), information which is contained in the period fluctuations seen in Fig. 6.

At the lowest preparation energy, at $\lambda = 585$ nm, the period starts near 290 fs and shows fluctuations of ± 20 fs. The latter are well within the definition of recursion times, therefore, in themselves, they are not very meaningful. The motion is essentially harmonic, with a trend of increasing period with time. A similar trend is observed for the 570 nm preparation. Clearly, the increase in period with time cannot be interpreted as the molecule gaining energy from the lattice. The more sensible interpretation is that the cage dilates as the molecule relaxes. As the site expands, the effective potential experienced by the molecule softens and the vibrational period stretches. This effect is observable in the low energy preparation, where the rate of energy flow from molecule to lattice is slow, yet the molecular motion is fast relative to the cage dilation time. In this limit, it is possible to estimate parameters of the sudden potential, and the effect of solvation. Thus, for the packets prepared at 570 and 585 nm, from the initial periods of nearly harmonic motion, frequencies of 111 and 115 cm^{-1} are obtained. Accordingly, the initial energy separation of 450 cm^{-1} between these two packets corresponds to 4 vibrations, and therefore, an anharmonicity of 0.5 cm^{-1} can be extracted for the sudden potential as compared to 0.8 cm^{-1} in the gas-phase *B*-potential.[41] Since in subsequent vibrations the periods of these two packets intersect, the oscillations of the cage toward its equilibrium geometry must produce a frequency modulation comparable to the 5% anharmonic difference between the two packets. Using the linear fit to the periods, after ~3 ps of evolution, the frequencies increase by ~1 cm^{-1}. Even if we ignore any vibrational relaxation, we may conclude that the solvation-induced anharmonicity (softening of the molecular spring) is larger than the anharmonicity of either the bare molecule, or the sudden potential.

3. Simulations

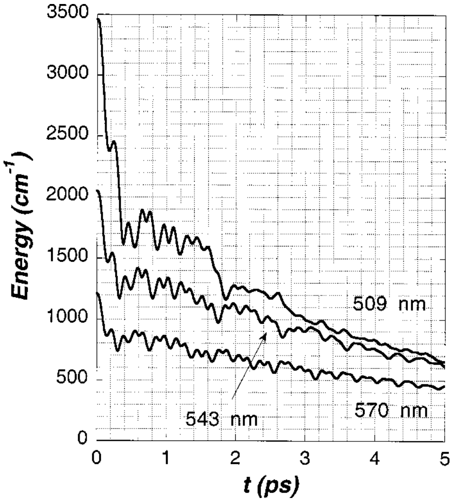

FIG. 7. Simulated energy loss in the *B*-state in Ar, for the indicated pump wavelengths.

As a guide to interpretations, we compare the experiments to prior molecular-dynamics simulations.[43] The extracted energy loss for three representative initial preparations is shown in Fig. 7, and the simulated periods are shown in Fig. 8. The periods of motion and the magnitude of their fluctuations are in good agreement with the experiment. However, the simulation fails to reproduce the cage dilation effect. In contrast with the experiments, even at 570 nm, energy dissipation dominates the periods. While the simulations fail in some details, they capture the general features of the dynamics. In particular, the nonlinear energy flow profile is in good agreement with the experiment. For example, we can estimate from the experiment that the 509 nm packet sheds more than 1000 cm^{-1} in vibrational energy in one period, since the second recursion in the 509 nm packet drops to 350 fs, equal to that of the first recursion at 537 nm. The simulation reproduces the same drop in period, and pins the energy loss to ~1700 cm^{-1} in the first cycle of motion. While qualitatively similar to $I_2(B)-\mathrm{Kr}$,[4] the nonlinearity of energy flow in Ar is more pronounced.

B. Dynamics on the cage-bound potentials

The pump–probe transients at $\lambda > 509$ nm while monitoring 380 nm emission, in Fig. 2, is strikingly different from those originating from the *B*-state (Fig. 1). The characteristic dynamics, which is best captured in the transient at 553 nm

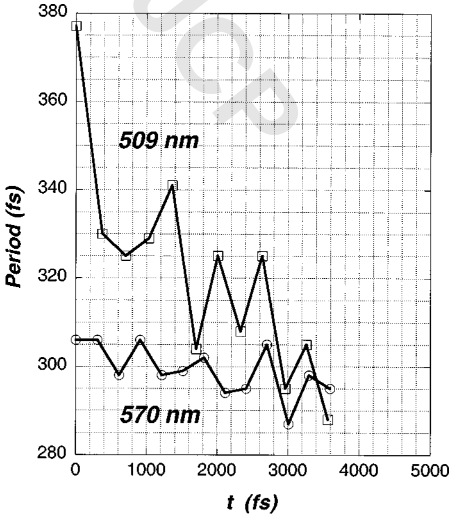

FIG. 8. Simulated periods of motion in the *B*-state for the indicated pump wavelengths.

is that of strongly damped oscillations. The first recursion occurs at 1.2 ps, with three subsequent oscillations at a period of 1 ps. The packet is fully dephased after the fourth recursion, near $t=4$ ps. The low frequency of these 35 cm^{-1} oscillations identifies the dynamics as motion on cage-bound potentials arising from dissociative molecular states. While the nature of the probed state is clear, a unique assignment to a single surface is difficult. We consider the spectroscopic arguments prior to analysis of the dynamics.

1. Spectroscopic considerations

The monitored emission at 380 nm is from the first tier of ion-pair states, previously assigned to $\mathrm{I}^+\mathrm{I}^-[D'(2g)] \rightarrow \mathrm{I}_2[A'(2u)]$.[1,32] The first tier ion-pair states can be located relative to the *B*-state in Ar, by noting that the emission carries the *B*-state signal at 509 nm but not at 525 nm (see Fig. 2). Based on the $\Delta\Omega=0$ propensity rule, the accessed ion-pair state can be identified as $E(0_g)$, and the threshold of the $\mathrm{I}^+\mathrm{I}^-[E(0_g)]\leftarrow \mathrm{I}^*\mathrm{I}[B(0_u)]$ transition can be located at 19 600 cm^{-1}. This is in acceptable agreement with the DIM potentials, which show a minimum separation between the *B* and *E* states of 20 250 cm^{-1} at $R=3.96$ Å.[28] Additionally, this establishes that population cascades within the tier, to radiate from the lowest D' state.

The longest wavelength at which the cage-bound motion is observed is at 585 nm. Assuming direct access, the probed state is ~2500 cm^{-1} closer to the first tier of ion-pair states than the *B*-state, uniquely placing it in the manifold of nine repulsive I*I potentials. This implies that the probed state is prepared by two-photon pumping, and this is consistent with experimental tests. It is difficult to further narrow the identity of the transitions. Under $\Delta\Omega=0$, ±1 selection rules, all I*I states are dipole coupled to one or more of the six ion-pair states in the first tier $[D'(2_g)$, $D(0_u^+)$, $E(0_g^+)$, $\beta(1_g)$, $\delta(2_u)$, $\gamma(1_u)$, in ascending order[37]$]$. If both $B\,^3\Pi(0_u^+)$ and $B'(^1\Pi_{1u})$ are considered as real intermediates in the two-photon preparation, dipole selection rules allow access to six states that correlate with I*I:$^3\Sigma_g^-(0^+,1)$, $^1\Delta_g(2)$, $^1\Pi_g$, $^3\Pi(0_g^+,0_g^-)$, three each arising from the 2422 and 2341 electron configurations,[31] respectively. According to Mulliken's energetics, which is maintained in the DIM construct, these states are clustered near 33 000–34 000 cm^{-1}. Once again, upward revision of potential walls by ~5000 cm^{-1} (at $R=2.67$ Å) is suggested. The strength of the transition relative to one-photon excitation of the *B*-state, suggests $\mathrm{I}^*\mathrm{I}[^3\Pi(0_g^+)]\leftarrow B[^3\Pi(0_u^+)\leftarrow X[^1\Sigma(0_g^+)]$ as the likely two-photon excitation channel.

2. Simulations

Following procedures that are well established,[1,2] we use classical molecular dynamics to simulate the pump–probe signals, to ascertain the above assignments, and to extract mechanistic details. For this purpose, we use a simulation cell consisting of three mobile layers of argon (218 atoms), surrounded by two stationary layers (664 atoms) of a perfect fcc lattice ($a_0=5.3$ Å). Iodine is introduced as a double substitutional impurity at the center of the cell. All interactions are described through pair-wise additive atom–atom potentials: Lennard-Jones ($\varepsilon=80.1$ cm^{-1}, $\sigma=3.40$ Å) for Ar–Ar interactions; Morse ($D_e=130.1$ cm^{-1}, $r_e=4.033$ Å, $\beta=1.586$ Å^{-1}) for I–Ar interactions, independent of electronic state.[44] An ensemble of 100 trajectories is used to simulate preparation at a particular pump wavelength, with initial coordinates and momenta Monte Carlo sampled from a lattice at $T=40$ K. The initial I–I bond-length is sampled in accordance with the Franck–Condon principle, assuming vertical two-photon excitation. To this end, the representative I*–I potential shown in Fig. 5(b) is constructed in Morse form, $D_e=297$ cm^{-1}, $r_e=4.25$ Å, $\beta=1.3822$ Å^{-1}, $T_e=20\,450$ cm^{-1}. In this construct, preparation at 500 nm corresponds to vertical access at $R=2.65$ Å; while 585 nm corresponds to $R=2.76$ Å. A representative set of trajectories, for excitation at 543 nm, is shown in Fig. 9. The observable signal is generated from the ensemble by modeling the probe pulse as a Gaussian window in coordinate and in time. The location and width of the window along the I–I coordinate are adjusted to reproduce the signal. Using the windows illustrated in Fig. 10, a good reproduction of the entire data set is obtained, as shown in Fig. 11(a). Additionally, to reproduce the experiments, the simulated signal amplitude is stepwise attenuated at the indicated times in Fig. 11. Given the faithful reproduction of the signal, we first consider the significance of the model parameters, followed by a discussion of the robust features of the underlying mechanics.

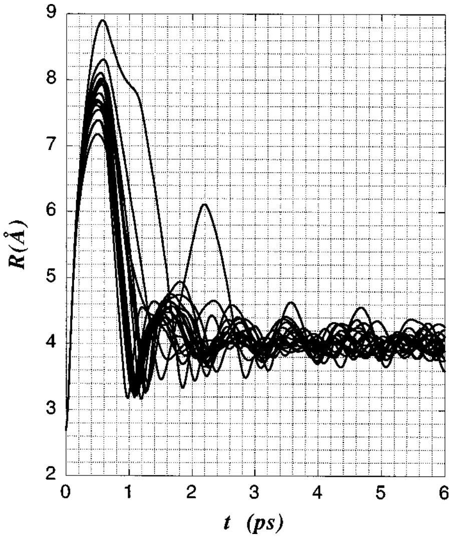

FIG. 9. Trajectory ensemble on the I*I potential, prepared by two-photon excitation at $\lambda=543$ nm (36 800 cm^{-1}), corresponding to an excess energy of 16 000 cm^{-1} on the I*I surface of Fig. 5(b).

In the static limit, the location of the probe window shown in Fig. 10 should trace the difference potential of the probe transition, $\Delta V(R)=V(I^+I^-)-V(I^*I)=E_{\text{probe}}$, and the width of the windows, $\Delta R(R^*)$, should be given by the curvature:

$$\Delta R(R^*)=\Delta E_{\text{probe}}\left.\frac{\partial(\Delta V)}{\partial R}\right|_{R^*}, \qquad (1)$$

in which ΔE_{probe} is the spectral width of the probe laser. The determined windows grossly follow the difference potentials for $\Delta\Omega=0$ transitions obtained from the sudden DIM poten-

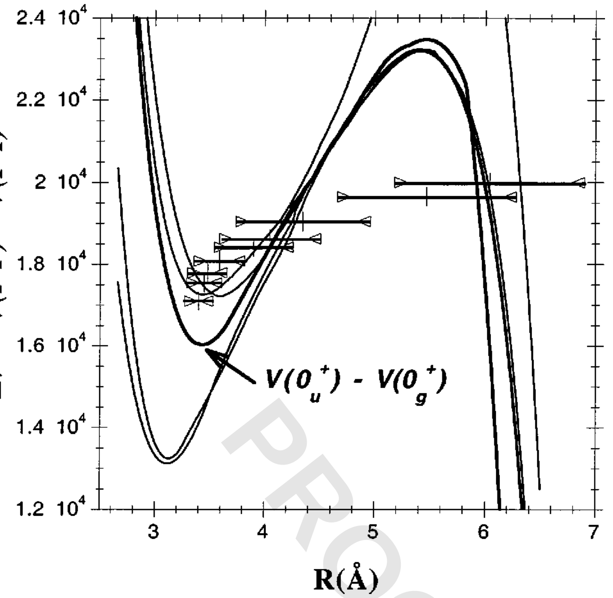

FIG. 10. The location and width of windows used in the simulations of Fig. 11(a), overlaid on the sudden difference potentials for $\Delta\Omega = 0$ transitions between I*I and ion-pair potentials of the first tier.

tials, as illustrated in Fig. 10. However, the required windows are significantly wider than what would be predicted from the spectral composition of the laser. The apparent inconsistency could signify that a band of difference potentials contributes to the signal, since through $\Delta\Omega = 0, \pm 1$ selection a given I*I potential is dipole coupled to several first tier ion-pair states. Or, if the packet evolves coherently on multiple I*I potentials after collision induced nonadiabatic transfer, then a band of difference potentials of rather similar shape would contribute to the probe window. More important is to note that the assumption of a static window is an approximation, especially when large amplitude motions are involved.[6] The resonances are dynamical, involving the solvation of both the probed state and the ion-pair terminus. The broad windows at $R > 5$ Å, suggests that the difference potential remains parallel, as would be expected if I–I interactions are turned off. Cognizant of these uncertainties, we restrict interpretations to the robust features.

The amplitude filtering required to reproduce the experiment is *compelling evidence of nonadiabatic dynamics*. This is clearest in the case of the transients at 500 and 509 nm in Fig. 2, in which the signal consists of a single peak at $t = 200$ fs (the subsequent modulation is from the *B*-state as discussed above). This signal is consistent with the passage of the outgoing trajectory flux through a probe window at 5 to 6 Å (see Figs. 9 and 10). Any such window must be re-crossed by the returning trajectories near $t = 900$ fs. Yet there is no trace of a recursion in the signal. The loss of flux cannot be due to unit dissociation probability, since contrary to the observations, this would lead to rapid permanent degradation of the sample. We must infer unit probability for curve crossing to a dark state at $R > 6$ Å. This probability diminishes from 1 at 509 nm, to 0.75 at 525 nm, to 0.60 at 543 nm. At longer pump wavelengths the returning trajectory flux is conserved—the signal amplitude is reproduced without introducing amplitude filters. We may infer the crossing to be at $R = 7.5$ Å, which corresponds to the maximum distance reached by 60% of the 543 nm trajectories. This nonadiabatic process must be assigned to collision induced spin-flipping, to transfer the population to one of the I– I potentials. Indeed, at $R \sim 7.5$ Å the repulsive walls I*I and I–I potentials merge (not shown in Fig. 5). Note, at these distances, the sudden potentials of Fig. 5 are not very meaningful. At the preparation energy of $\sim 37\,000$ cm^{-1}, the outer turning point of the sudden I*I and I–I potentials merge near $R = 5.5$ Å, a distance much shorter than $R = 7.5$ Å reached

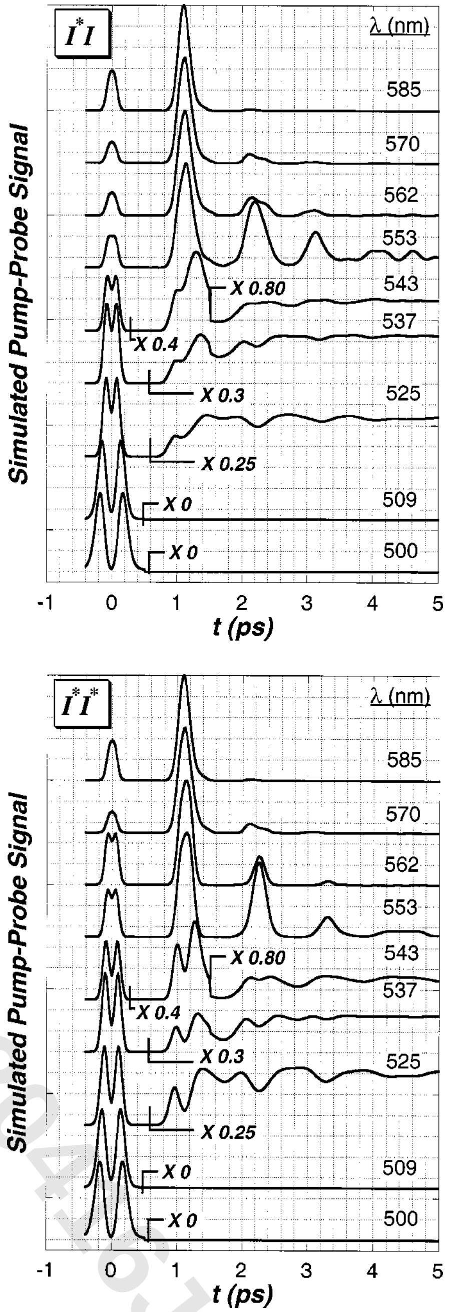

FIG. 11. (a) Simulated pump–probe signal from the I*I cage-bound potential of Fig. 5(b). The experimental signals are reproduced when the indicated amplitude filters are used. The loss of trajectory flux indicates nonadiabatic curve crossing. (b) Simulated pump–probe signal from the I*I cage-bound potential of Fig. 5(b).

by the trajectories in the initial stretch (see Fig. 9). As the I atoms push against the Ar cage, the I–Ar interaction changes from J–J to Λ–Σ coupling, and the I(1/2) and I(3/2) curves cross.[45,46] With the help of the trajectories, we can accurately establish that the spin–flip occurs during $\Delta t < 300$ fs that marks the turning of the corner, after being last seen at $t = 200$ fs near $R = 6$ Å. Also, the simulations imply that the 543 nm flux is further lost near $t = 1.5$ ps, where $R \sim 4.5$ Å. Inspection of the potential in Fig. 5(a) identifies the likely channel in this case to be nonadiabatic transfer from cage-bound I*I to I*I(B), the latter being the only I*I potential where the population can fall out of the observation window. This crossing does not occur along the sudden I–I coordinate according to Fig. 5(a). The coupling must be inferred to be host induced, with a crossing along a driven I_2-cage coordinate as in the more carefully analyzed case of solvent-induced predissociation of $I_2(B)$.[26]

Consider the mechanics of the strongly driven cage. The first recursion time shows a small, monotonic increase from 1.22 to 1.24 ps for the range $\lambda = 585$–537 nm. Thus, for an initial excess energy increasing by as much as 1500 cm^{-1}, the rebound time of the cage stretches only by ~2%. Since these are single color measurements, the observed recursion time can be effected by the change in the probe window position. The simulations make it clear that this is not a significant consideration. In the same energy range, the simulations show a first recursion time of 1.1 ps, with negligible dependence on excess energy. At 500 nm, where the experiment is silent due to curve hopping, the simulation yields a recursion time of 1.2 ps. Moreover, in this ensemble of 20 000 cm^{-1} excess energy, 3% of the trajectories show dissociation. Thus, we may associate 1.2 ps with the rebound time of a cage driven to the point of breaking. In good agreement with the experiments, the second recursion drops to 1 ps, and to the extent that it can be defined, the period remains constant in subsequent recursions. The subsequent three oscillation periods are most clearly assignable in the 553 nm data. However, even then, in contrast to motion on the bound B-state, the packet dephases in three periods, as can be discerned from the trajectories in Fig. 9. Despite the dispersion of the packet, the motion is harmonic, even though the molecule has stretched from its initial equilibrium bond length in $I_2(X)$ of 2.67–4 Å on the I*I surface. The characteristic cage mode that modulates the I–I internuclear separation at $\omega = 33\ \mathrm{cm}^{-1}$ ($\tau = 1$ ps), must be characterized as a resonant local mode. The mass difference between impurity and host is sufficient to rationalize this frequency. Thus, using $[m(\mathrm{I})/m(\mathrm{Ar})]^{1/2} = 1.78$, the resonant mode can be connected to a lattice mode at 58 cm^{-1}, near the Debye edge of Ar (65 cm^{-1}). That this regular motion appears already in the second period, while we know that the lattice is overdriven initially far beyond its harmonic limit, illustrates the rapid decay of the slew of phonons generated in the initial impulse. Shock waves are an obvious means for efficient transport of the impulsive excitation.[18–20]

3. Sensitivity to choice of potentials

It is useful to question as to what extent are the above findings specific to the choice of potential? The question is particularly significant, since the data do not allow a unique assignment of the I*I potential. To address this issue, we repeat the simulations on an effective potential representative of I*I*. This potential was parametrized as a Morse, to resemble the I*I*(0_g^+) with its experimentally suggested correction of the repulsive wall: $r_e = 4.25$ Å, $D_e = 297\ \mathrm{cm}^{-1}$, $\beta = 1.2139$ Å^{-1}, $T_e = 28\,050\ \mathrm{cm}^{-1}$ [see Fig. 5(b)]. Since the electronic origin of this potential is shifted upwards by the spin–orbit splitting of $\Delta = 7600\ \mathrm{cm}^{-1}$, the excess energy at which packets are launched at a given pump wavelength is now reduced by Δ. Since this potential is forced to be two-photon accessible in the same experimental range, this surface shows a softer repulsive wall than the I*I potential. Following the same procedure as above, adjusting probe window locations and widths, and introducing amplitude filters, the experimental data can be reproduced with fidelity comparable to the simulations on I*I, as shown in Fig. 11(b). Based on the simulated signal alone, it is difficult to favor one potential over the other. The main difference between the two sets of trajectories can be understood in terms of the reduced excess energy. Now the dispersion of trajectories is smaller, the ensemble is more coherent, and the resonances are sharper in the pump–probe signal. This is in part compensated in the simulations by adjusting the probe window width. The periods of motion are insensitive to the dramatic change made in the energetics. Indeed, the reduction in kinetic energy leads to a reduced amplitude of motion. For example, when prepared at 537 nm, the initial stretch on the I*I surface reaches R_{max}=8 Å, while on the I*I* surface it reaches R_{max}=6.5 Å. Both of these distances are far beyond the right turning points of the sudden potentials at this energy (which occur near $R = 5.5$ Å). Given the large amplitude of the initial stretch, where I*–Ar and I–Ar potentials are strongly mixed, the spin–flipping probabilities inferred from the amplitude filters used in the reproduction of the signal are as sensible on the I*I* surface as on the I*I surface. The justification of the second filter applied to the 543 nm trajectories (20% reduction at $t = 1.5$ ps) is less obvious now. However, this alone does not seem sufficient to discount the candidacy of the I*I* surface.

We also tested the sensitivity of results to the I–Ar interaction. No appreciable difference in the dynamics and in the simulated signal was observed when we changed the range parameter, β, of the I–Ar potential by 3%. Finally, we tested the effect of the Ar–Ar interaction. Born–Mayer potentials were used; $U_{\mathrm{Ar-Ar}} = A\exp(-\alpha r - \beta r^2) - C/r^6$, with parameters $A = 24\,951\,000\ \mathrm{cm}^{-1}$, $\alpha = 2.864$ Å^{-1}, $\beta = 0.1415$ Å^{-2}, $C = 431\,000\ \mathrm{cm}^{-1}$ Å^6 obtained by fitting Aziz's Hartree–Fock dispersion potential,[47] which is considered to be accurate in describing short-range Ar–Ar repulsion. This pair potential has a softer repulsive wall than the Lennard-Jones at energies above 1000 cm^{-1}. The trajectories and the simulated signals were not affected noticeably. Further softening the Ar–Ar potential, by reducing the repulsive range parameter by 0.1 Å, produced a noticeable change in the dynamics. Using this softer potential for the matrix atoms, the maximum I–I separation at the first collision with the cage grew by more than 0.5 Å. The timing of the first recursion grew from 1.1 to 1.2 ps, in closer agreement with

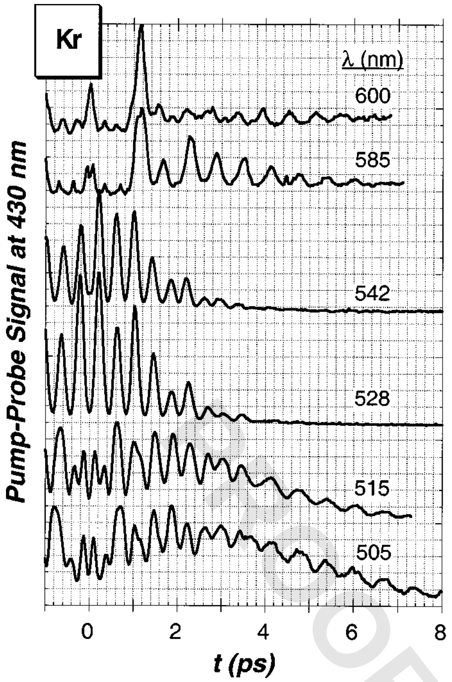

FIG. 12. Single color pump–probe measurements of $I_2-Kr(s)$, while monitoring the ion-pair emission at 430 nm. The data set parallels that of I_2-Ar shown in Fig. 2. At $\lambda=585$ nm, the signal is from cage-bound motion. At $\lambda=542$ the signal is strictly from the *B*-state. At $\lambda\leqslant 515$ nm, the initial modulation is due to a packet on the *B*-state, while the modulation at $t\geqslant 4$ ps is due to cage-bound motion.

the experiment. Also, the swarm became more dispersed. The latter effect is difficult to quantify without having independent input on probe window parameters.

In summary, our analysis shows that the pump–probe signal from cage-bound potentials is most sensitive to the choice of the repulsive wall of the Ar–Ar potential, and both rebound and subsequent recursion periods are surprisingly insensitive to the initial preparation energy of the chromophore. The observed dynamics is generic of cage-bound potentials, determined primarily by the dynamics of the host cage rather than the chromophore. It is, therefore, instructive to consider the host effect on this motion.

4. Host dependence: Kr

In Fig. 12 we show a stack plot of single color pump–probe measurements carried out in Kr, while monitoring the $D'\rightarrow A'$ ion-pair emission at 430 nm. Except for the 585 and 600 nm traces, which were withheld, this data set has been previously presented and discussed in some detail.[6] The trend of wavelength dependence in the full set closely parallels that of Ar shown in Fig. 2. At 542 nm, the signal shows a regular periodicity of 400 fs, arising from wavepacket motion on the *B*-state, probed via $E\leftarrow B$ excitation on the attractive wall of the potential. At 585 nm, the *B*-state contribution is minor (identified by the black dots in Fig. 12). Now, in analogy with the Ar discussion, the principle signal must be assigned to cage-bound motion. The outgoing packet can be seen at $t=80$ fs, the rebound occurs at $t=1.15$ ps, followed by damped oscillations with a period of 630 ± 20 fs. In comparison to the stack plot of Ar, the 1200 cm^{-1} red shift in the appearance of this signal in Kr is due to the differential solvation of the *E*-state in the more polarizable host.[32,35] In analogy with the Ar analysis, the 585 and 600 nm signals may be assigned to motion on spin-excited dissociative potentials accessed by two-photon pumping. The rebound time in Ar and Kr are strikingly similar. However, the subsequent period of oscillation is significantly shorter in Kr (630 fs vs 1 ps) and the packet dephases after 8 cycles, vs 3 cycles in Ar.

At 528 nm, the *B*-state signal occurs over a flat baseline. At 515 and 505 nm, it rides over a background that peaks near 3 ps. Moreover, the periodicity of the signal suddenly switches from the *B*-state value of 350 fs to 630 ± 30 fs at $t=4$ ps. We have previously assigned the latter to cage motion.[6] However, under the assumption that the signal is from the *B*-state, we had suggested that it could only survive if driven by an accidental two-to-one resonance between the molecule and the cage belt. The suggestion is superfluous if signals from two different potentials are being observed, as we must conclude from the observation that the same periodic motion can be observed without exciting the *B*-state (585 and 600 nm data). That motion on two different potentials is being monitored has also been argued by Schwenter *et al.*[11–14] We must conclude that the persistent oscillations at $\omega=53\ \mathrm{cm}^{-1}$ ($\tau=630$ fs) are due to cage-bound motion. However, the identity of the potentials is less clear. Given the extent of the coherence out to $t=8$ ps, the population must have been created suddenly, therefore, not consistent with trickle-down through predissociation of the *B*-state. Given the absence of the most prominent signatures of a strictly cage-bound motion, namely the peaks at $t=0$ and $t=1.2$ ps that arise from the initial stretch and rebound, it is clear that this state is not directly accessed. Notably, in both the 505 and 515 nm traces where the persistent oscillations are observed, signal at the second period of motion on the *B*-state, at $t=700$ fs, is abnormally high. This is the time at which the trajectories turn the corner at the cage wall (see Fig. 9), where the spin–flip occurs as discussed above. Thus, the interpretation that is most consistent with all observations is that the observed oscillations are the result of population on a cage-bound I–I potential, which is nonadiabatically, but suddenly, prepared on its right turning point near $t=700$ fs. Based on energy conservation alone, the state must be probed via two-photon access of the ion-pair states. Note, of the ten potentials that merge at the I–I asymptote, the bound *X*, *A*, and A' states can be eliminated. Also, the $B'(1_u)$ state can be eliminated, since if it were due to direct access to this state then the rebound at 1.2 ps would be visible.

We carry out a normal mode analysis to ascertain the assignment and the nature of the 53 cm^{-1} oscillations. To this end, we use a 108-atom lattice with an iodine molecule in a double substitutional site. For the dissociative I–I interaction we use the same potential used in the molecular-dynamic (MD) simulations above: A Morse potential with a 300 cm^{-1} well at 4.25 Å. Lennard-Jones potentials for Kr–Kr,[42] and isotropic Morse potentials for I–Kr interactions are assumed.[10] After simulated annealing of the solid, the normal modes are computed by diagonalizing the Hessian. In the relaxed lattice, the I–I distance is 4 Å, determined by the cage rather than the assumed van der Waals

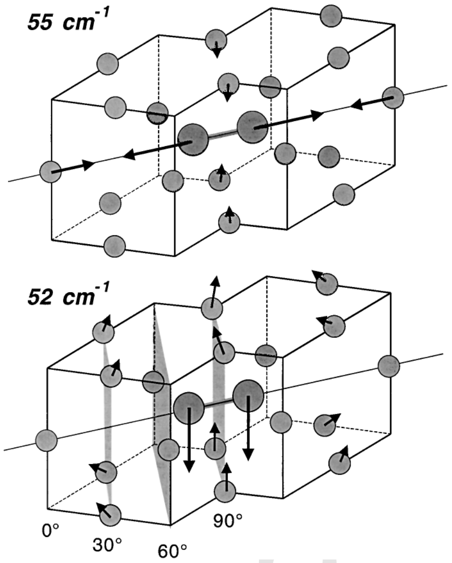

FIG. 13. Local modes on cage-bound potentials. The immediate cage consists of 18 atoms, which are categorized by the angle they span relative to the I–I internuclear axis. Atoms carrying greater than 3% of the vibrational amplitude are decorated with arrows. The highest frequency normal local mode is the stretch-belt motion at 55 cm^{-1}. The rest of the local modes consist of either center of mass motion of I_2, as in the depicted 52 cm^{-1} mode, or librations.

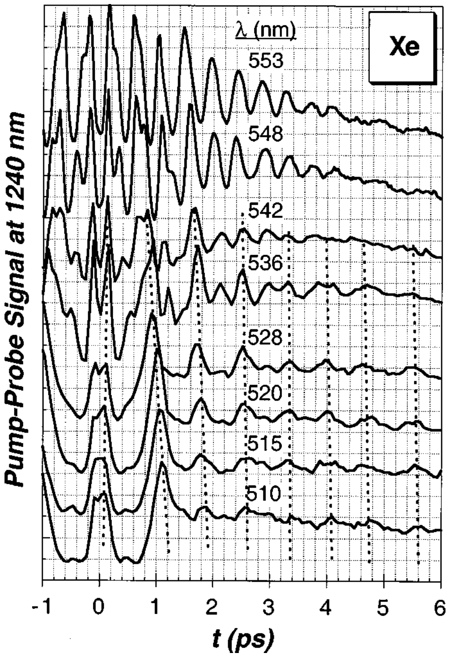

FIG. 14. Single color pump–probe measurements of $I_2-Xe(s)$, while monitoring the spin–flip transition at 1240 nm. The dotted lines serve as a guide to connect the cycles of motion on the cage-bound potential. At 548 and 553 nm, the modulation is from the *B*-state, except for the last two week cycles, which show the cage-bound motion period of $\tau = 800$ fs.

well. In this lattice, six localized modes appear, with amplitude >10% localized on the two I atoms, near the Debye limit of 50 cm^{-1}.[42] The highest frequency mode, at 55 cm^{-1}, is the I–I stretch accompanied by the belt compression. The mode is illustrated in Fig. 13. In this local mode, 23% of the amplitude is localized on the two I atoms, 12% on the two axial Kr atoms, 13% on the four belt atoms, and the eight Kr atoms at 30° carry 21% amplitude (not shown). In the remaining five local modes, three involve center of mass translation of the I–I pair, and two are librational. The second highest frequency local mode, at 52 cm^{-1}, involves translation of the I–I pair against the belt ring, as illustrated in Fig. 13. In this case, 13% of the amplitude is localized on the two I atoms, 16% is on the four belt atoms, and 23% is on the eight Kr atoms at 30°. The delocalized phonons, in which less than 1.5% of the amplitude is on a given I atom, occur below 48 cm^{-1}. The only local mode that can effectively modulate the electronic transitions of the chromophore is the 55 cm^{-1} stretch-belt motion, which given the approximate nature of the used pair interactions should be regarded as in good agreement with the observed 53 cm^{-1} oscillations. The persistent cage oscillations in Kr can be unambiguously assigned to localized vibrations on cage-bound potentials.

5. Host dependence: Xe

A set of single color pump–probe measurements in Xe, obtained by monitoring the spin-flip transition at 1240 nm,[38] is shown in Fig. 14. At 553 and 548 nm, the oscillatory signal with a period of $\tau \sim 400$ fs, is due to a wavepacket on the *B*-state. The same holds up to $\lambda = 580$ nm,[7] placing the $E \leftarrow B$ gap near 17 500 cm^{-1}. The $\sim$2000 cm^{-1} reduction in the gap relative to Ar is consistent with the expected magnitude for dielectric solvation of ion-pair states.[35,48] The first tier ion-pair states do not radiate in Xe. They predissociate via I*I*,[38] whence the emission is monitored (This fact has been neglected in Ref. 34, leading to the missassignment of the ion-pair states in Xe, and the unreasonable conclusion that they blue-shift relative to Kr, back to the energy in Ar.) For $\lambda < 528$ nm, the characteristic signal for cage-bound motion can be seen: First recursion at $t = 1.1$ ps and subsequent oscillations at $\tau = 800$ fs (42 cm^{-1}). At 542 nm the signal has contributions from both packets. At 536 nm, while the contamination from the *B*-state is small, the signal shows period doubling characteristic of a probe window located at the bottom of the potential. A similar data set has been published already, in which the observed motion was ascribed to I*I, with the suggestion that the packet reaches there via nonadiabatic transfer from the *B*-state.[7] The latter suggestion can be refuted based on the observation of the outgoing packet near $t = 0$, and on two-color measurements that show the *B*-state population to be conserved.[49] Here too, two-photon access of the spin-excited potentials is the more likely pumping scheme. Independent of a specific state label, the dissociative nature of the molecular potentials on which the packet moves is clear. The observed 42 cm^{-1} motion can be safely assigned to the localized vibration on the cage-bound potential. Given the similarity of masses, and the fact that the Xe–Xe potential is nearly identical to the mean of Xe–I* and Xe–I interactions,[50] the I–I stretch on the dissociative potential should be nearly identical to the Debye frequency of the pure solid of 44 cm^{-1}.[42]

In their simulations of nonadiabatic dynamics in liquid Xe, at $\rho^* = 1$, Batista and Coker present trajectories of motion on dissociative potentials, which oscillate with a period of 800 fs as in the present.[51] This, we remark, to underscore the generic nature of strictly cage-bound oscillations.

C. The breaking of the cage

In contrast with Kr and Xe matrices, in our time-resolved studies of I_2 in Ar, we observe permanent degradation of the signal with time. While we have not carried out systematic wavelength dependence studies, the process has been observed throughout the visible spectral range and at wavelengths as long as 800 nm. In all tested cases, the multiphoton nature of the dissociation process is clear, even though a direct power dependence analysis fails, often yielding fractional powers. An approximate analysis of the depletion curves shown in Fig. 4 has already been given. A more rigorous analysis of the photoselective multi-photon dissociation kinetics is given in the Appendix. There, we show that depletion curves obtained by the sequential irradiation cycles of a given volume with cross-polarized beams is a powerful method for obtaining photodissociation and detection cross sections, and their orders in irradiation intensity. The measurement is sensitive to overlap of the beam volumes, and the intensity profile of the laser must be included in the analysis. The analysis identifies the photodissociation as three-photon induced, and the detection as two-photon limited, with both processes being dominated by parallel transitions. Note, the monitored 380 nm fluorescence in these single beam measurements is from the ion-pair states, which can only be accessed by three-photon excitation. The measurement does not identify a unique channel. We rely on simulations for mechanistic insights.

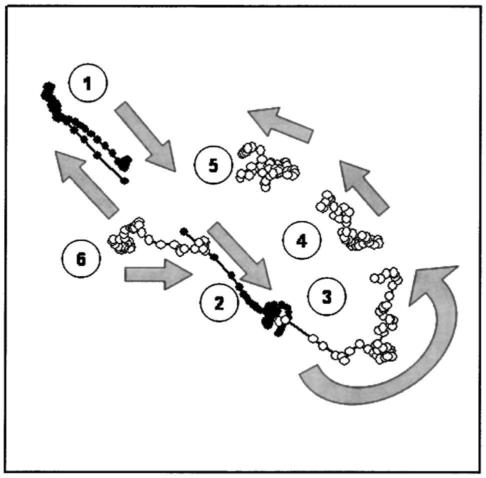

FIG. 15. Ballistics of cage breakout. The black dots represent I atoms, while the white circles represent Ar atoms. The positions are recorded at fixed intervals, such that the separation between positions reflects relative velocity. Four Ar atoms are displaced during the photodissociation.

We assume a shallow Morse potential for the I–I interaction, with parameters $D_e = 297\ \mathrm{cm}^{-1}$, $r_e = 4.25\ \text{Å}$, $\beta = 1.4896\ \text{Å}^{-1}$, to represent the unbound I–I interaction [see Fig. 5(b)]. Dissociation yields are then studied systematically in a wide range of initial excess energies. At each energy, a swarm of 200 trajectories was propagated for 5 ps, using a simulation cell with four mobile layers (448 argon atoms) and one additional frozen layer. Dissociation of the molecule was diagnosed by the final I–I separation, whether it exceeded the nearest-neighbor distance in argon (3.75 Å). The final I–I distances were found to fall into three distinct groups: (a) $R \sim 3.75\ \text{Å}$, indicating nondissociation, (b) $R \sim 2 \times 3.75\ \text{Å} = 7.5\ \text{Å}$, indicating cage exit of one of the I atoms with an intervening Ar atom preventing recombination; (c) $R \sim 3 \times 3.75\ \text{Å} = 11.25\ \text{Å}$, resulting from both I atoms exiting the cage. In all cases a direct cage exit mechanism is observed, one in which upon first collision the I atom dislodges an Ar atom, which in turn embeds itself interstitially into the lattice and drives one or more Ar atoms out of their equilibrium positions. In all cases, the separated iodine atoms remained aligned along the original molecular direction, they did not rotate around each other, indicating that the massive projectiles plow their way through the relatively soft lattice. A typical example of a single-exit event is illustrated in Fig. 15, in which only atoms that are involved in large amplitude motions (>1 Å) are shown. In this case, initially both I atoms exit the cage. One bounces back and thermalizes in the original site (atom 1). The second iodine atom (atom 2), impulsively drives an Ar atom (atom 3) into the lattice, which in turn displaces other Ar atom (atoms 4 and 5). In the region shown at the right top corner of the figure, the cage is substantially perturbed, with an excess argon atom (atom 5) interstitially trapped. We can also see that the site originally occupied by the second iodine is back-filled with an argon atom (atom 6) after some thermal incubation, leaving a vacancy behind. This atom prevents thermal recombination of the molecule. The cage is broken, with significant disturbance of the lattice caused by multiple atom displacements. The breaking of the cage is triggered by the probability that upon impact with an iodine atom, one of the axial cage atoms be impulsively driven into the lattice. This initiates the disruption that leads to permanent dissociation. In many respects, the observed process is akin to the high energy, direct channel of dissociation of Cl_2 in solid Ar.[52]

The excess energy dependence of the probabilities for single and double exit is given in the bar graph of Fig. 16, for an initial lattice temperature of 40 K. We also computed the exit probabilities in a 20 K lattice, where dissociation probabilities were found to be systematically smaller. The temperature dependence has a simple mechanistic origin. To drive an axial cage atom into the lattice, the atom–atom collisions must not be collinear. The larger the amplitude of

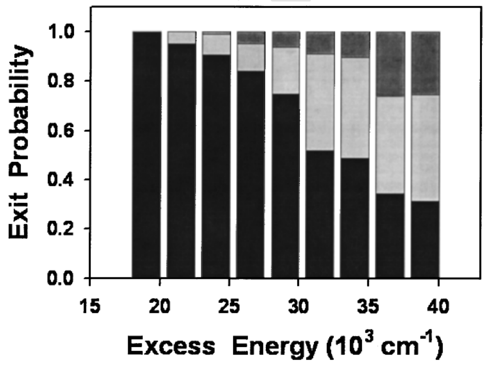

FIG. 16. Photodissociation quantum yield as a function of excess energy on the I–I potential. The bar–graph illustrates the probabilities of no dissociation (black), single cage exit (light gray), and double exit (dark gray).

atom motion, the larger the probability of noncentral collisions, hence the increased dissociation probability with temperature. The alignment of cage atoms relative to the lattice controls the probabilities of the different channels of Fig. 16. Dissociation yields reach 60% at excess energies of 35 000 cm^{-1} (4.4 eV), at $T=40$ K. The same probability is observed in the 20 K lattice at an excess energy of 5.2 eV. At 550 nm, the excess energy available via three-photon access of the dissociative I–I potentials is 5.4 eV, while three-photon access of the I*I potential leads to an excess energy of 4.4 eV. Thus, the observed three-photon induced permanent decay of the signal occurs at experimentally accessible energies, and therefore, provides a consistent rationale for the observed polarization selective permanent depletion of the molecules.

Indirect confirmation of the above model is found in recent vacuum ultraviolet (VUV) investigations of the ion-pair states, in which it was observed that 193 nm excitation leads to efficient bleaching of the absorption bands in Ar, but not in Kr.[35] This excitation energy corresponds to an excess of 5.1 eV on the I–I potential, therefore near unit quantum efficiency of dissociation is predicted for the nonradiative molecules. It was also noted that the bleaching of the absorption bands do not occur with a single rate. The red edge of the absorption depletes first, and the rest of the band decays on a slower time scale.[35] It is tempting to assign such an observation to molecules in different sites. Our analysis suggests the alternate interpretation that anisotropic bleaching is being observed. Unless measurements are carried out with depolarized optics, the sample will develop dichroism: The parallel bands will lose intensity relative to the perpendicular bands. Indeed, the red-most absorption in the UV is expected to be the parallel $D \leftarrow X$ transition, with the perpendicular $\gamma \leftarrow X$ transition only slightly shifted to the blue (the electronic origin of the γ-state is estimated to be 600 cm^{-1} above the D-state[37]). This interpretation also suggests the utility of polarization selective bleaching as means to disentangle overlapping broad resonances.

V. CONCLUSIONS

A rather complete picture of driven cage dynamics is obtained through the pump–probe measurements of I_2 isolated in solid Ar. Particularly insightful in this regard is the dynamics observed on cage-bound potentials, to which the majority of covalent potentials of I_2 belong. This class of wavepacket dynamics was identified and analyzed in Ar through simulations; and was extended to re-interpret previously observed cage motion in Kr,[6,14] and in Xe.[7] On dissociative, cage-bound potentials, the molecule acts as a transducer to drive the cage into large amplitude motion and to passively report the subsequent rebound and ringing of the cage as it relaxes. The rebound time, determined by the collective host interactions, is surprisingly insensitive to the amplitude of the initial drive, up to the breaking point of the cage. Immediately after rebound, the coherent oscillations of the impurity induced local modes are observed. Due to the mass asymmetry in Ar, a resonant cage mode at 33 cm^{-1} arises. In Kr and Xe, the local mode frequencies of 53 and 41 cm^{-1}, remain at the Debye edge of the respective hosts. The coherence of the cage-bound wavepackets, therefore of the driven local modes, decays on time scales of 3 ps in Ar, and 6–8 ps in Xe and Kr. These oscillations in Kr were recently attributed to zone-boundary phonons excited by the intact molecule.[14] Our analysis of the dynamics and of the normal modes in Kr, clearly show that the observed motion must be ascribed to local modes on dissociative surfaces.

The quantitative analysis of the cage-bound dynamics reveals nonadiabatic spin–flip transitions, which reach unit probability when the molecular bond is stretched beyond 6 Å. The process is sudden, limited to the outer turning point of the initial stretch. The persistent cage oscillations that accompany the B-state signal in Kr, can clearly be identified as the result of a wavepacket created through this sudden nonadiabatic transition. Although not surprising, it is useful to recognize that coherence can survive sudden, nonadiabatic transitions in condensed media.

In the gentle excitation regime, deep in the bound B-state, the suddenly accessed potential is observed to fluctuate as it dilates to its final equilibrium position. The accommodation occurs on the time scale of 3 ps, namely the ringdown time of the cage observed on the dissociative surface. The analysis quantifies the evolution of the molecular spring constant from that of the sudden cage, determined by the ground state lattice configuration, to that of the relaxed cage. When prepared near the dissociation limit of the B-state, after a dramatic energy loss in one period, the molecule falls deep into the bound part of the potential and undergoes nearly linear dissipation. Although overshadowed by the dissipative molecular vibrations, the cage oscillations can clearly be identified as fluctuations in the molecular period of motion. The entire process follows the pattern of dynamics on the cage-bound potentials, clearly establishing the latter as the generic cage response to impulsive excitation. We would have expected the same dynamics to be observable in the studies where the cage is driven through Rydberg excitations of a trapped impurity.[15–17] The conclusion from those studies seems to suggest that the cage response is overdamped, except in one report where the published trace shows 2 to 3 oscillations with a period of 900 fs,[53] characteristic of a gently driven Ar cage.

The photodissociation of iodine in Ar involves the breaking of the cage. This is distinct from the common mechanism in which the dissociation is principally that of cage exit of a fragment, by passing over the potential barrier provided by cage atoms.[8] In this case, the I atoms destroy the cage by driving axial cage atoms into the lattice, and getting trapped in the vacancies they create. The process occurs when excess energy of ~4 eV is deposited in the molecule. While the exact path on potential energy surfaces is not clear, the experiments establish that the process is driven by three visible photons, which would provide the required energy to break the cage. Dissociation of I_2 in Ar and Ne was also reported in studies where the same amount of energy was directly deposited through UV excitation.[34]

We have given an explicit treatment of the kinetics of multiphoton photoselective photodissociation, which could be expected to be ubiquitous in systems in which the chromophore does not rotate. We emphasize that in such a treatment both the angular and spatial anisotropy of the radiation must be included. The nonexponential decay curves, in which the rate dramatically decelerates, can otherwise be mistaken for bimolecular (or higher order) kinetics.

Finally, an intimate part of time-dependent studies is the characterization of energetics, namely the potentials. This is contained in spectroscopic assignments, and where dynamical resonances associated with large amplitude motions are reproduced, significantly more information about energetics is obtained than through frequency domain spectra, which report a narrow range of stationary points. For example, the spectral analysis of emission spectra of cage-bound potentials report difference potentials over a range of 0.1 Å.[10] The present dynamical analysis reports difference potentials over several Ångstrom. We establish the energetics of the E state in Ar, Kr, and Xe, and establish that it follows the expected trend of solvation of ion-pair states. Although the E state in Xe is located via $E \leftarrow B$ excitation, no emission can be seen from the first tier of ion-pair states. They predissociate via the I*I* potentials. In Ar, beside the first tier $D' \rightarrow A'$ transition, emission from the second tier $f(0_g)$ and $F(0_u)$ ion-pair states is observed and assigned. These assignments are in variance with the recent frequency domain studies.[34,35]

ACKNOWLEDGMENTS

This research was made possible through a grant from the USAFOSR (F49620-01-1-0449). We would like to thank V. Batista and D. Coker for making available to us their DIM sudden potentials of iodine in matrices. Stimulating discussions with N. Schwentner and M. Bargheer are fondly appreciated.

APPENDIX A

In samples where the chromophore may not rotate, photodissociation with polarized radiation necessarily proceeds with nonexponential kinetics. Where nonlinear excitation is involved, in addition to the angular anisotropy of decay rates, it is essential to take the laser field intensity distribution into account. When explicitly treated, the sequential recording of kinetic curves from the same irradiation volume using cross-polarized beams is a rather complete experiment that can yield absolute cross sections. The specific case we consider, multi-phonon dissociation detected through multi-photon induced fluorescence, should be common when using short intense pulses in systems with dense electronic manifolds.

We assume optically thin samples of thickness l, and irradiation perpendicular to the film with linearly polarized light. Then for a volume element in cylindrical geometry, $\pi r l dr$, taken to be small enough to be subject to homogeneous irradiation intensity, $I(r)$, the angularly anisotropic rate equation for dissociation via m-photon excitation is

$$\frac{1}{\rho^0(r,\Omega)}\frac{d\rho(r,\Omega)}{dt} = -\sum_{i,j} \sigma_i^{(m)}(\Phi_{i,j}^2 I_j(r))^m, \tag{A1}$$

in which $\Phi_{i,j}$ is the direction cosine between the transition dipole, $i=x,y,z$, in the molecular frame and the polarization vector, $j=X,Y,Z$, in the laboratory frame; and $\sigma^{(m)}$ is the cross section for dissociation via m-photons (the product of m-photon absorption and quantum yield of dissociation). The time dependence of the differential element for a linear molecule subject to Z-polarized irradiation is

$$\rho(r,\Omega,t) = \rho^0(r,\Omega)\exp[-I(r)_Z^m(\sigma_\parallel^{(m)}\cos^{2m}(\vartheta) + \sigma_\perp^{(m)}\sin^{2m}(\vartheta))t]. \tag{A2}$$

In which ϑ is the polar angle between the molecular axis, z, and the polarization vector, Z. Note, the assumption of m-photon parallel and perpendicular cross sections is an approximation that ignores the possibility of alternating transition dipoles over intermediate resonances.

The same excitation source is also used for detection, now through an n-photon induced fluorescence. Assuming that the fluorescence is detected through a polarization scrambler (the inclusion of polarization selective detection is straightforward), the observable signal from the differential element can be written in the same vein

$$S(r,\Omega,t) = [I(r)_Z^n(\sigma_\parallel^{(n)}\cos^{2n}(\vartheta) + \sigma_\perp^{(n)}\sin^{2n}(\vartheta))]\rho(r,\Omega,t). \tag{A3}$$

Taking the laser intensity distribution to be Gaussian with beam wait w

$$I(r) = I_0 \exp\left(-\frac{r}{w}\right)^2. \tag{A4}$$

The observable signal is obtained by integrating over the Euler angles and over the irradiation area

$$S(t) = \int d\Omega \int dr S(r,\Omega,t) r. \tag{A5}$$

Beside the laser profile, which is characterized separately, the function contains six independent variables: The orders for dissociation and detection, m and n, and the parallel and perpendicular cross sections associated with each. Although perfect fits of the experimental signal is possible, given the large number of variables the choice of the best fit model is based on small preferences in fitness.

A more stringent test is provided when considering the sequential irradiation cycles, which does not add any new variables but provides additional observables. After an irradiation period τ, the polarization is rotated from Z to X in the laboratory frame

$$\rho(r,\Omega,\tau+t) = \rho(r,\Omega,\tau)\exp[-I(r)_X^m(\sigma_\parallel^{(m)}\Phi_{zX}^{2m} + \sigma_\perp^{(m)}(1-\Phi_{zX}^2)^m)t], \tag{A6}$$

where

$$\Phi_{zX}^2 = \cos^2(\vartheta)\sin^2(\varphi). \tag{A7}$$

The signal from the differential element

$$S(r,\Omega,\tau+t) = [I(r)_Z^n(\sigma_\parallel^{(n)}\Phi_{zX}^{2n} + \sigma_\perp^{(n)} \times (1-\Phi_{zX}^2)^n)]\rho(r,\Omega,\tau+t), \tag{A8}$$

is then integrated as in (A5) to obtain the decay curve over the second cycle, $S(\tau+t)$.

The nonexponential decay of the first cycle can be fitted extremely well with our model assuming only parallel transitions with third-order dissociation and second-order detection mechanisms. This model also gives a reasonable fit for the second cycle, although differences in absolute intensities and experimental sensitivities with respect to the two perpendicularly polarized beams that are not accounted for in our model, make it less quantitative. The fit shown in Fig. 4 is a compromise, overall fit of the two cycles. Knowing the energy (450 nJ), the duration (40 fs) and repetition rate (1000/s) of the pulses and the diameter of the focal region (35 microns), using our fit we can extract a three-photon, parallel dissociation cross section of 10^{-81} $\mathrm{cm}^6\ \mathrm{s}^2$. While we know energetically that to observe UV fluorescence from the ion-pair states in a single beam excitation, three-photons are required, the analysis yields a two-photon cross section. Indeed, the transition dipole to the ion-pair states is expected to be 2 to 3 orders of magnitude larger than the transitions within the covalent manifold, and as such the last transition is expected to be saturated. This suggests that the three-photon excitation that leads to dissociation is not via the ion-pair states, but rather via the dissociative repulsive wall of states in the same region that correlate with ground state I atoms.

[1] R. Zadoyan, Z. Li, C. Martens, P. Ashjian, and V. A. Apkarian, Chem. Phys. Lett. **218**, 504 (1994).
[2] Z. Li, R. Zadoyan, V. A. Apkarian, and C. C. Martens, J. Phys. Chem. **99**, 7453 (1995).
[3] R. Zadoyan, Z. Li, C. C. Martens, and V. A. Apkarian, J. Chem. Phys. **101**, 6648 (1994).
[4] R. Zadoyan, M. Sterling, and V. A. Apkarian, J. Chem. Soc., Faraday Trans. **92**, 1821 (1996).
[5] C. J. Bardeen, J. Che, K. R. Wilson, V. V. Yakovlev, V. A. Apkarian, C. C. Martens, R. Zadoyan, B. Kohler, and M. Messina, J. Chem. Phys. **106**, 8486 (1997).
[6] R. Zadoyan, J. Almy, and V. A. Apkarian, J. Chem. Soc., Faraday Trans. **108**, 255 (1997).
[7] V. A. Apkarian, J. Chem. Soc., Faraday Trans. **108**, 334 (1997).
[8] N. Schwentner and V. A. Apkarian, Chem. Rev. (Washington, D.C.) **99**, 1481 (1999).
[9] M. Karavitis, Z. Bihary, and V. A. Apkarian, Low Temp. Phys. (to be published).
[10] M. Karavitis and V. A. Apkarian, J. Phys. Chem. B **106**, 8466 (2002).
[11] M. Bargheer, K. Donovang, P. Dietrich, and N. Schwentner, J. Chem. Phys. **111**, 8556 (1999).
[12] M. Bargheer, M. Gühr, P. Dietrich, and N. Schwentner, Phys. Chem. Chem. Phys. **4**, 75 (2002).
[13] M. Gühr, M. Bargheer, P. Dietrich, and N. Schwentner, J. Phys. Chem. A **106**, 12002 (2002).
[14] M. Gühr, M. Bargheer, and N. Schwentner, Phys. Rev. Lett. (to be published).
[15] M. T. Portella-Oberli, C. Jeannin, and M. Chergui **259**, 475 (1996).
[16] C. Jeannin, M. T. Portella-Oberli, S. Jimenez, F. Vigliotti, B. Lang, and M. Chergui, Chem. Phys. Lett. **316**, 51 (2000).
[17] S. Jimenez, M. Chergui, G. Rojas-Lorenzo, and J. Rubayo-Soneira, J. Chem. Phys. **114**, 5264 (2001).
[18] A. Borrmann and C. C. Martens, J. Chem. Phys. **102**, 1905 (1995).
[19] A. Cenian, S. Hennig, and H. Gabriel, J. Chem. Phys. **102**, 9276 (1995).
[20] A. Cenian and H. Gabriel, J. Phys.: Condens. Matter **13**, 4323 (2001).
[21] J. Frank and E. Rabinowitch, Trans. Faraday Soc. **30**, 120 (1934).
[22] A. Harris, J. Brown, and C. Harris, Annu. Rev. Phys. Chem. **39**, 341 (1988).
[23] N. F. Scherer, D. M. Jonas, and G. R. J. Fleming, Chem. Phys. **99**, 153 (1993).
[24] C. Lienau and A. H. Zewail, J. Phys. Chem. **100**, 18629 (1996).
[25] Q. Liu, C. Wan, and A. H. Zewail, J. Phys. Chem. **100**, 18667 (1996).
[26] R. Zadoyan, M. Sterling, M. Ovchinnikov, and V. A. Apkarian, J. Chem. Phys. **107**, 8446 (1997).
[27] N. Yu, C. J. Margulis, and D. F. Coker, J. Phys. Chem. B **105**, 6728 (2001).
[28] V. S. Batista and D. F. Coker, J. Chem. Phys. **106**, 6923 (1997).
[29] M. Bargheer, M. Y. Niv, R. B. Gerber, and N. Schwentner, Phys. Rev. Lett. **89**(10), 108301 (2002).
[30] M. Bargheer, R. B. Gerber, M. V. Korolkov, O. Kuhn, J. Manz, M. Schroder, and N. Schwentner, Phys. Chem. Chem. Phys. **4**, 5554 (2002).
[31] R. S. Mulliken, J. Chem. Phys. **55**, 288 (1971).
[32] M. Macler and M. C. Heaven, Chem. Phys. **151**, 219 (1991).
[33] S. Fei, X. Zheng, M. C. Heaven, and J. Tellinghuisen, J. Chem. Phys. **97**, 6057 (1992).
[34] J. Helbing and M. Chergui, J. Chem. Phys. **115**, 6158 (2001).
[35] J. Helbing and M. Chergui, J. Lumin. **94**, 611 (2001).
[36] V. S. Batista and D. F. Coker, J. Chem. Phys. **105**, 4033 (1996).
[37] For the gas phase characterization of the ion-pair states, see: J. C. D. Brand and A. R. Hoy, Appl. Spectrosc. Rev. **23**, 285 (1987).
[38] A. V. Benderskii, R. Zadoyan, and V. A. Apkarian, J. Chem. Phys. **107**, 8437 (1997).
[39] M. Karavitis, R. Zadoyan, and V. A. Apkarian, J. Chem. Phys. **114**, 4131 (2001).
[40] Z. Bihary, M. Karavitis, R. B. Gerber, and V. A. Apkarian, J. Chem. Phys. **115**, 8006 (2001).
[41] G. Herzberg, *Spectra of Diatomic Molecules* (Van Nostrand Reinhold, New York, 1950).
[42] C. Kittel, *Introduction to Solid State Physics*, 5th ed. (Wiley, New York, 1976).
[43] Z. Bihary, M. Karavitis, and V. A. Apkarian, J. Phys. Chem. (to be published).
[44] Parameters used in the vibrational self-consistent field analysis of overtones in solid Ar are given in, Z. Bihary, R. B. Gerber, and V. A. Apkarian, J. Chem. Phys. **115**, 2695 (2001).
[45] P. Casavecchia, G. He, R. K. Sparks, and Y. T. Lee, J. Chem. Phys. **77**, 1878 (1982).
[46] T. Lenzer, M. R. Furlanetto, N. L. Pivonka, and D. M. Neumark, J. Chem. Phys. **110**, 6714 (1999).
[47] R. A. Aziz, J. Chem. Phys. **99**, 4518 (1993).
[48] M. E. Fajardo and V. A. Apkarian, J. Chem. Phys. **85**, 5660 (1986); **89**, 4102 (1988).
[49] Unpublished data.
[50] W. G. Lawrence and V. A. Apkarian, J. Chem. Phys. **101**, 1820 (1994).
[51] Fig. 12(c) in Ref. 36.
[52] R. Alimi, R. B. Gerber, J. G. McCaffrey, H. Kunz, and N. Schwentner, Phys. Rev. Lett. **69**, 856 (1992).
[53] M. Chergui, J. Chem. Soc., Faraday Trans. **108**, 341 (1997).